Machine learning-based interatomic potential development and phase transition analysis of ferroelectric hafnium dioxide

Yasantha Hetti Kankanamalage [1,2,*] Yufeng Xi [3] Shuai Zhang [2] Sobhit Singh [1,3] and Niaz Abdolrahim [1,2,3]

[1]*Department of Mechanical Engineering, University of Rochester, Rochester, New York 14627, USA*

[2]*Laboratory for Laser Energetics, University of Rochester, Rochester, New York 14623, USA*

[3]*Materials Science Program, University of Rochester, Rochester, New York 14627, USA*

(Received 8 August 2025; accepted 5 January 2026; published 29 January 2026)

The ferroelectric phase ($Pca2_1$, which is in orthorhombic symmetry) of hafnium dioxide (HfO_2) has gained much attention due to its potential applications in nanoelectronics and advanced memory devices. However, its complex phase behavior under external stimuli, such as pressure and temperature, remains a subject of intense investigation. This study focuses on developing a machine learning-based interatomic potential (MLIP) that is trained with data from density-functional theory (DFT) calculations to simulate phase transitions and mechanical properties of HfO_2. The developed MLIP predicts lattice parameters, equations of state, bulk and shear moduli, and elastic constants that closely align with DFT predictions for several phases and at various pressures. Once validated, the MLIP is used to investigate the phase transitions of ferroelectric HfO_2 ($Pca2_1$) under both isobaric and constant stress conditions at elevated temperatures ranging from 200 to 2500 K. We used several complementary methods, including local symmetry identification, radial distribution function, and x-ray diffraction characterization, to identify interesting phase transitions among several competitive hafnia phases predicted from our simulations. The suggested methods uniformly reveal that under pure deviatoric condition, the system favors a transition from the orthorhombic $Pca2_1$ phase to a tetragonal ($P4_2/nmc$) phase, whereas a zero stress condition drives the system from the $Pca2_1$ phase to another orthorhombic ($Pbcn$) phase. These findings provide crucial insights into stress and temperature-induced phase behavior of hafnia, guiding future experimental and theoretical studies for optimizing hafnia-based ferroelectric devices.

DOI: 10.1103/gkvf-t1vl

I. INTRODUCTION

Ferroelectric hafnia (HfO_2) has emerged as a leading candidate for next-generation nanoelectronic and nonvolatile memory applications due to its robust polarization, scalability, and complementary metal–oxide–semiconductor (CMOS) compatibility [1,2]. The ferroelectric phase of HfO_2 is attributed to a metastable polar orthorhombic structure (space group $Pca2_1$) and shows a switchable remanent polarization up to 50 $\mu C/cm^2$ in hafnia thin films [3–6]. This property underlies a broad array of technologies such as advanced nonvolatile memories and ultra-low-power logic [7]. Compared to traditional materials like lead zirconate titanate, HfO_2 offers significant advantages, including excellent compatibility with CMOS technology [8], scalability via atomic layer deposition [9], and an environmentally friendly, lead-free composition. Interesting properties of hafnia can also be finely tuned through chemical doping and strain, allowing for enhanced flexibility in application-specific optimization [10,11]. It is therefore important to evaluate the stability of ferroelectric HfO_2 at elevated temperatures to ensure the retention of polarization across relevant temperature–pressure regimes. In addition, it enables low-power logic devices, supports energy harvesting and storage through its piezoelectric and pyroelectric behavior, and finds use in sensors, neuromorphic computing, and radio frequency/microwave technologies [12,13]. However, despite these promising attributes, the ferroelectric properties of the $Pca2_1$ phase can be sensitive to external conditions such as temperature and pressure. Understanding how these factors influence the stability and transition pathways of the ferroelectric phase is critical for optimizing its functional performance in real-world applications.

This study focuses on the $Pca2_1$ phase and examines how this ferroelectric phase transitions into nonferroelectric phases under increased temperatures and controlled pressure conditions. To accurately model these structural transformations and their underlying mechanisms, reliable computational methods such as molecular dynamics (MD) that can look into atomistic configurations are essential. In MD simulations, the interactions between atoms are described by interatomic potentials or force fields, which significantly influence the accuracy of simulated structural transitions. The development of accurate interatomic potentials is, therefore, the core of atomistic simulations in materials science, as they determine the energy landscape that governs atomic interactions. Traditional empirical potentials, while computationally

*Contact author: yhettika@ur.rochester.edu

efficient, often lack the precision required to capture complex bonding environments, limiting their applicability to specific materials and conditions. For example, a well-known TiO_2 potential (Matsui–Akaogi type) incorrectly predicts a hypothetical pyrite-type TiO_2 phase to be stable over a large pressure range, even though that phase has not been observed experimentally [14]. Also, in another study focusing on ZrO_2, authors note that "no empirical interatomic potential is capable of seamlessly describing all phases [of ZrO_2], nor to reach such accuracy" as their machine learning-based interatomic potential [15]. Given that HfO_2 belongs to the same class of binary transition metal oxides as TiO_2 and ZrO_2, it shares similar complexities in its phase behavior. In contrast, first-principles methods like DFT are highly precise but are significantly computationally expensive for large-scale simulations. To bridge this gap, machine learning approaches have recently emerged as a promising alternative, enabling the construction of interatomic potentials that combine the accuracy of quantum mechanical calculations with the efficiency of empirical models. This motivates us to adopt a machine learning (ML)-based interatomic potential specifically tailored for HfO_2. MD simulations conducted with our newly developed interatomic potential reveal that varying pressure conditions can induce different phases of HfO_2, which highlights the sensitivity of its phase behavior to the applied thermodynamic constraints, especially how stress is controlled during the simulation.

In this paper, we first report the development of a deep-learning-based interatomic potential for HfO_2 using DFT data from a wide range of pressure and temperature configurations. Then, we validate the new potential against known structural, mechanical, and thermodynamic properties across several crystalline phases of HfO_2, showing its accuracy. We then apply the developed potential to investigate the high-temperature phase transitions of $Pca2_1$-HfO_2 in MD simulations. To do that, we employed two ensembles for stress-controlled simulations: the isobaric ensemble and the constant stress ensemble, as described in the LAMMPS documentation [16]. In the isobaric ensemble, we only define the scalar pressure without specifying the individual stress components, i.e., $P = (\sigma_{xx} + \sigma_{yy} + \sigma_{zz})/3 = 0$. However, individual stress components may not necessarily be zero, thus representing a deviatoric stress state. In contrast, in the constant stress ensemble, individual components of the stress tensor are explicitly defined, i.e., $\sigma_{xx} = \sigma_{yy} = \sigma_{zz} = 0$, which corresponds to a zero-stress state. These simulations allowed us to investigate the behavior of the ferroelectric phase of HfO_2 under different stress control schemes at elevated temperatures.

Phase identification during temperature-induced transitions in HfO_2 is challenging because several metastable polymorphs can emerge under similar thermodynamic conditions [17,18]. A common approach in the literature is to infer the post-transition phase from changes in lattice parameters or oxygen-atom displacements associated with ferroelectric behavior; yet this strategy becomes unreliable in large-scale MD simulations, where the cell frequently breaks into coexisting domains of different phases rather than remaining uniform. Under such conditions, the averaged lattice constants no longer represent any single phase accurately, thereby masking local transitions and obscuring the true phase landscape. Moreover, focusing solely on ferroelectric behavior can also be misleading: for example, both *Pbcn* and tetragonal ($P4_2/nmc$) polymorphs of HfO_2 exhibit no net polarization, and therefore one could easily misassign these phases interchangeably based on average net polarization alone. To avoid such confusion, it is essential to complement bulk measurements with techniques that resolve subtle symmetry differences to unambiguously distinguish among these closely related pure HfO_2 phases. The crystal structures of the $Pca2_1$, $P4_2/nmc$, and *Pbcn* phases considered in this work are shown in Fig. 1.

Here, we employ three complementary techniques to identify HfO_2 phases: a machine-learning–based local symmetry identification model to capture atomic-scale heterogeneity, radial distribution function (RDF) analysis for local structural ordering, and an x-ray diffraction (XRD) classification model for the overall crystallographic structure. Together, these methods provide both local and global insights into the phases present in the system, yielding a comprehensive and precise phase assignment.

Our simulations reveal that increasing the temperature drives the transition from the polar $Pca2_1$ phase to higher-temperature, nonpolar phases. However, the exact phase transition pathway depends on how stress is applied during the simulations. Simulations in the isobaric ensemble reveal that the $Pca2_1$ phase transitions into a mixture of tetragonal and *Pbcn* phases, with a high concentration of the tetragonal phase. In contrast, the constant-stress ensemble suggests that $Pca2_1$ mainly transitions into a mixture dominated by the *Pbcn* phase. In previous studies [19], the tetragonal phase was frequently identified as the high-temperature product without specifying how the stress was controlled. However, our simulations indicate that deviatoric components of the stress tensor play a crucial role in determining the energy pathway the material follows.

Previous first-principles investigations by Fan *et al.* [20] combined DFT calculations with finite-temperature MD using deep-potential models trained on different exchange–correlation functionals in the NPT ensemble. They found that, with models trained on DFT data using the Perdew–Burke–Ernzerhof (PBE) generalized gradient approximation (GGA) functional, the system transforms from the $Pca2_1 \rightarrow Pbcn$ phase at around 950 K, whereas models trained on the PBE for solids (PBEsol) functional yield a $Pca2_1 \rightarrow P4_2/nmc$ transition. Remarkably, under the same stress conditions, both their PBE results and our MD simulations yield the $Pca2_1 \rightarrow Pbcn$ transition at a similar critical temperature. In contrast, by employing a dataset generated with the same PBE functional, we found that selectively controlling the applied stress can also drive the same phase transition, without altering the exchange–correlation functional. Our MD simulations reveal an alternative $Pca2_1 \rightarrow P4_2/nmc$ pathway that is accessed solely by controlling the stress, thereby achieving both structural endpoints through stress control rather than through the choice of functionals in DFT calculations. We note that the results obtained from our constant-stress ensemble are in complete agreement with those of Fan *et al.* Moreover, a key new finding of this work is that the system can also be driven toward the tetragonal phase by appropriately con-

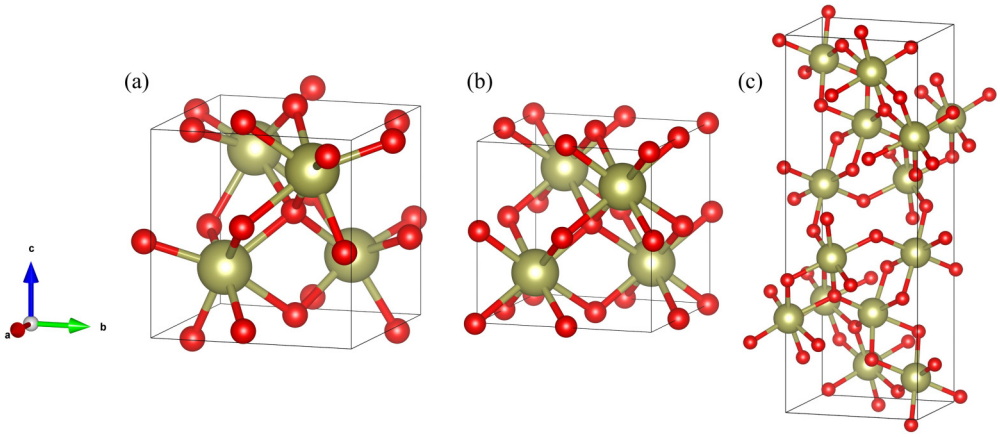

FIG. 1. Crystal structures of different phases of HfO_2: (a) Ferroelectric Orthorhombic ($Pca2_1$) phase, (b) Tetragonal ($P4_2/nmc$) phase, and (c) Orthorhombic ($Pbcn$) phase. Gold spheres represent Hf atoms, and red spheres represent O atoms. The $Pca2_1$ phase exhibits a noncentrosymmetric structure with spontaneous polarization, while the $P4_2/nmc$ and $Pbcn$ phases are centrosymmetric and nonpolar. The $Pbcn$ phase is considered the parent structure of $Pca2_1$ connected through a soft polar mode [2], highlighting their structural relationship.

trolling the applied stress. Complementing these findings, Wu *et al.* [21] have recently shown that deep-learning interatomic potentials can faithfully reproduce temperature-induced phase transitions in HfO_2, lending further validation to our simulation of the polar orthorhombic ($Pca2_1$) to nonpolar phase transformation.

II. RESULTS AND DISCUSSIONS

In this section, we first discuss the development of our machine learning-based interatomic potential (MLIP) for HfO_2 and show its evaluations on different benchmark tests. Secondly, we discuss the MD setup for temperature ramping simulations and the three methods we used for robust phase identification. Finally, we discuss the influence of stress states on the resulting phases based on our observations and analysis of the simulations. Also, we discuss our results from the free energy and enthalpy calculations of the two ensembles at comparable temperatures. For a detailed explanation on methods, please see Sec. IV.

A. Machine learning interatomic potential

The MLIP model for hafnium and oxygen atoms was trained using DeepMD-kit [22] on a DFT dataset (≈30 000 simulation frames) covering a wide range of temperatures and pressures. The training data were obtained from a public data repository [23] and include DFT molecular dynamics trajectories for four distinct phases of HfO_2; further details about the dataset are provided in the Computational Methods section. The model employed neural network architectures and was optimized on energy, force, and virial contributions during the training process, achieving strong accuracy and reliable predictions. The model was evaluated with different HfO_2 phases, including unseen crystal structures, to verify its performance and transferability. Below, we show the evaluation of the potential through a series of benchmarks, including lattice parameters, equations of state, shear and bulk moduli, and the elastic constants of the $Pca2_1$ phase under different pressures.

In addition to those benchmarks, we also note that experimental RDFs or structure factors specifically for the crystalline phases of HfO_2 that we chose to study in this work ($Pca2_1$, $Pbcn$, and $P4_2/nmc$) are extremely limited in the literature, mainly due to their metastability. However, for the tetragonal ($P4_2/nmc$) phase, we can estimate bond lengths from the reported experimental lattice parameters in Refs. [24,25] and the known Wyckoff positions. From these calculations, we obtain an Hf–O short bond of 2.09–2.12 Å and an Hf–O long bond of 2.23–2.35 Å. The bond-length analysis from our simulations at a comparable temperature (∼2000 K) agree reasonably well with these experimentally derived values (see Fig. S12 in the Supplemental Material [26]).

1. Lattice parameters

To determine the lattice parameters a, b, and c for various phases of HfO_2, we performed simulations using LAMMPS [27], ensuring full structural relaxation at 0, i.e., simultaneous relaxation of atomic positions, cell shape, and volume, at 0 K temperature and 0 GPa pressure. Notably, even though $Fm\bar{3}m$ and $Pbcn$ phases were excluded from the training dataset, our developed machine learning interatomic potential predicted their lattice parameters with a minimal error of 1.02% and the maximum percentage error across all phases is less than 1.2%, as shown in Table I. For the lattice angles (α, β, γ), every phase shows 90°—except the monoclinic ($P2_1/c$) phase, where $\alpha = \gamma = 90°$ and $\beta = 99.56°$—and in all cases, these predicted angles are consistent with DFT values. DFT calculations were also performed at 0 K and 0 GPa conditions with the PBE exchange-correlation functional.

2. Equations of state

For validating our developed MLIP, we computed the equation of state (energy versus volume) for each HfO_2 polymorph using supercells of $6 \times 6 \times 6$ unit cells in LAMMPS. This involved isotropically scaling the relaxed structure across a range of volumes and calculating the corresponding total energies. The resulting data (shown in Fig. 2) were fitted to the third-order Birch-Murnaghan equation of state, a standard

TABLE I. Comparison of lattice parameters (a, b, c) for different phases of HfO_2, as predicted by our MLIP (shown in bold) versus reference DFT values. For each parameter, the table also reports the percentage error of the MLIP prediction relative to the DFT benchmark. Space group $Fm\bar{3}m$ and *Pbcn* (shown in bold) were not included in the training dataset. Experimental values found for some phases are indicated in parenthesis: *—[28]; △—[29]; □—[30]; ⊕—[31].

	$P2_1/c$	*Pbca*	$Pca2_1$	$P4_2/nmc$	$\boldsymbol{Fm\bar{3}m}$	***Pbcn***	
	5.146	5.265	5.265	5.075	5.067	4.81	*DFT benchmark (this work)*
	(5.116)*	—	(5.228)△	(5.061)□	(5.115)⊕	—	*Experiment*
a (Å)	**5.140**	**5.243**	**5.265**	**5.069**	**5.075**	**4.859**	*MLIP (this work)*
	−0.12%	−0.42%	0.00%	−0.12%	0.16%	1.02%	*Percentage error*
	5.154	10.094	5.047	5.075	5.067	5.78	*DFT benchmark (this work)*
	(5.172)*	—	(5.003)△	(5.061)□	(5.115)⊕	—	*Experiment*
b (Å)	**5.175**	**10.038**	**5.042**	**5.069**	**5.075**	**5.824**	*MLIP (this work)*
	0.41%	−0.55%	−0.10%	−0.12%	0.16%	0.76%	*Percentage error*
	5.352	5.078	5.078	5.279	5.067	15.92	*DFT benchmark (this work)*
	(5.295)*	—	(5.059)△	(5.201)□	(5.115)⊕	—	*Experiment*
c (Å)	**5.322**	**5.078**	**5.077**	**5.216**	**5.075**	**16.033**	*MLIP (this work)*
	−0.56%	0.00%	−0.02%	−1.19%	0.16%	0.71%	*Percentage error*

model for pressure–volume–energy relationships under compression [32]. We extracted DFT EOS data from Ref. [19] for every phase except *Pbcn*. Since that reference does not report *Pbcn* data, we carried out our own DFT calculation for this phase. Across the $P2_1/c$, $P4_2/nmc$, *Pbca*, and $Pca2_1$ phases—and the held-out *Pbcn* and $Fm\bar{3}m$ phases (not included in training)—the MLIP-derived EOS curves closely match the DFT results, demonstrating both accuracy and transferability beyond the training set.

3. Shear and bulk moduli

The bulk modulus (B) and shear modulus (G) for six different phases of HfO_2 were calculated using our developed MLIP and are summarized in Fig. 3. All simulations were performed at 0 K and 0 GPa. The elastic constants C_{ij} were obtained by computing the second derivative of strain energy. (see Sec. IV B for more details). We included the *Pbcn* phase and the $Fm\bar{3}m$ phase—both absent from the training dataset—to evaluate the model's predictive performance on previously unseen HfO_2 structures. The low percentage errors observed for these two phases highlight the strong transferability of the MLIP.

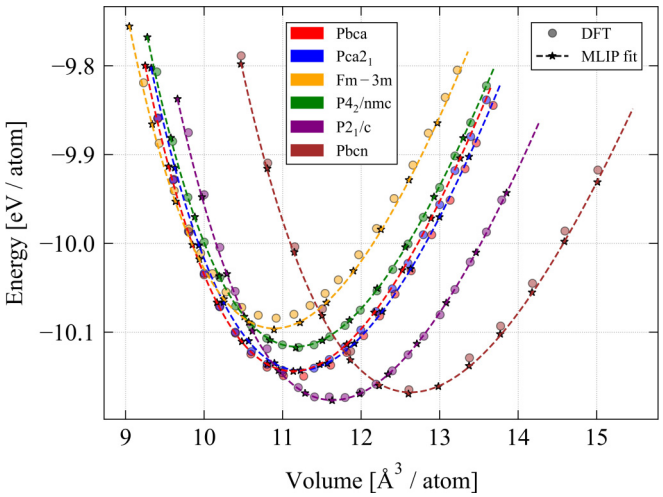

FIG. 2. Equations of state (energy vs volume) for HfO_2 polymorphs: *Pbca*, $Pca2_1$, $Fm\bar{3}m$, $P4_2/nmc$, $P2_1/c$, and *Pbcn*. Circular markers show DFT reference data, while star markers indicate calculations from the developed MLIP. The third-order Birch–Murnaghan fits to the MLIP data are also shown as dashed curves. The close agreement between MLIP and DFT curves across all volumes highlights the MLIP's accuracy in reproducing the DFT equation of state. Note that $Fm\bar{3}m$ and *Pbcn* phases were not included in the training set.

4. Elastic constants of $Pca2_1$ phase at high pressure regions

The elastic constants C_{ij} of the $Pca2_1$-HfO_2 phase were computed using the MLIP by applying controlled strains to a

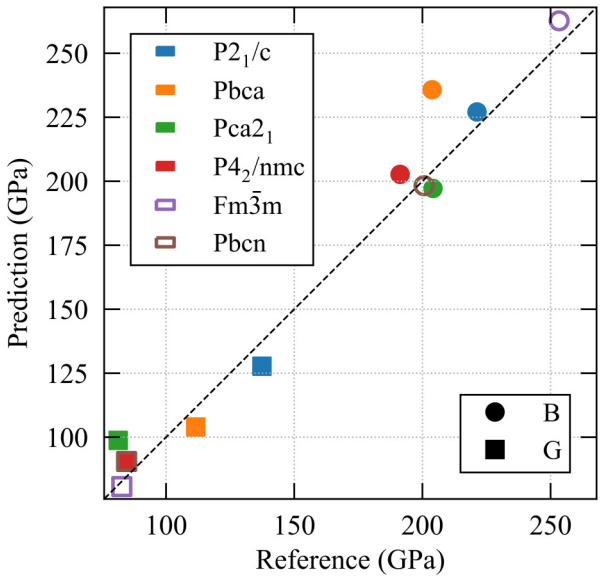

FIG. 3. Predicted bulk modulus (B) and shear modulus (G) from the MLIP model compared against DFT reference values for six HfO_2 polymorphs. All quantities were computed at 0 K and 0 GPa. DFT reference values are taken from Ref. [19]. The *Pbcn* and $Fm\bar{3}m$ phases—denoted by open symbols—were not included in the MLIP training dataset, showing the model's transferability to previously unseen structures.

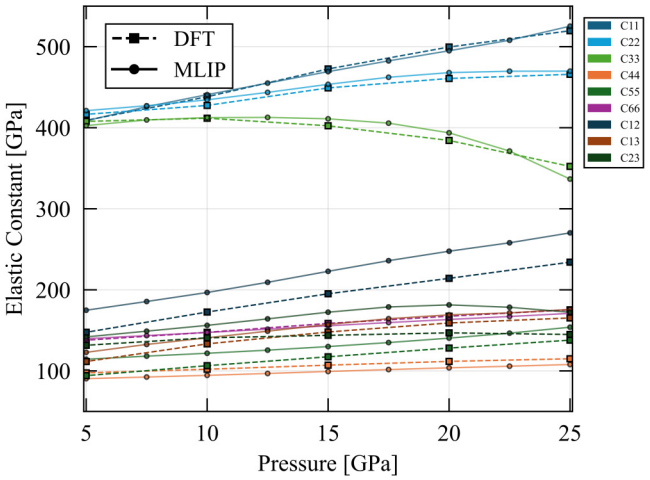

FIG. 4. Pressure dependence of the nine independent elastic constants C_{ij} of the $Pca2_1$ phase of HfO_2. DFT results are shown as dashed lines with square markers, while MLIP predictions are solid lines with circle markers. Line colors identify each C_{ij} component as listed in the right legend.

supercell of $6 \times 6 \times 6$ unit cells in LAMMPS and then fitting the resulting energy–strain data to the strain energy function [Eq. (3)]. An identical protocol was carried out with DFT in VASP, using a 12-atom unit cell and $8 \times 8 \times 8$ Monkhorst–Pack k-mesh. In both cases, structures were relaxed to the target pressures before performing the C_{ij} calculations. A more detailed description of this procedure is provided in the Computational Methods section.

Based on our analysis of the elastic properties (Fig. 4), we observe that the MLIP predictions generally reproduce the DFT results within an error margin of less than 15%. When comparing our MLIP-predicted elastic constants to DFT values, a discrepancy of less than 15% is considered reasonable and acceptable. This is primarily because the AIMD training dataset was obtained from a public data repository [23] and was not generated by us; the exact computational parameters used in its generation—such as k-point sampling, smearing schemes, force-convergence thresholds, or pseudopotentials—are not fully documented. In contrast, our reference DFT calculations for evaluating the elastic constants were performed independently, attempting to match the original AIMD dataset settings as closely as possible. Therefore, minor differences between the training and evaluation protocols can naturally lead to small deviations in elastic moduli. Overall, these results indicate that the MLIP reliably captures the underlying elastic behavior at a fraction of the computational cost.

The decrease in the C_{33} component in Fig. 4 is caused by the anisotropic displacement of certain oxygen atoms in the crystal structure of ferroelectric HfO_2 under increasing pressure, as discussed in Ref. [33]. The reduced resistance around these atoms allows them to shift from the vertical direction (z axis) to the horizontal plane, weakening the bonds along the z axis and leading to a significant softening of C_{33}. This behavior indicates potential structural instability and a possible phase transition at higher pressures [34].

B. Phase transitions in HfO_2

1. Temperature ramping MD simulations

We performed MD simulations using the LAMMPS [27] software package and visualized the results using OVITO [35]. The simulations used a time step of 1 fs. For both isobaric and constant-stress simulations, a Nosé-Hoover thermostat with a temperature damping constant of 100 fs and a Nosé-Hoover barostat with a pressure damping constant of 1000 fs were used. We employed supercells of $8 \times 8 \times 8$ unit cells in each ensemble. In both cases, the temperature was equilibrated for 30 ps at each step before being gradually increased by 200 K over a 20 ps period. The equilibrated systems served as the starting points for the subsequent temperature ramps, ensuring smooth temperature increments. The simulations started at an initial temperature of 0 K and ramped up to a final temperature of 2000 K for both pressure-control methods. The simulations were initiated with the $Pca2_1$ phase of HfO_2 at 200 K and 0 GPa. Throughout the simulations, the pressure was maintained at 0 GPa. However, two different ensembles, namely isobaric and constant-stress, were employed to control the system's pressure.

2. Phase detection

Determining the phase of HfO_2 at elevated temperatures is challenging, primarily due to thermal fluctuations and the appearance of multiple metastable phases under these conditions. Such challenges are also present in dynamic compression scenarios, where the phase transformation pathway can be highly sensitive to factors like stress state, strain rate, and crystallographic orientation—as demonstrated in aluminum under ramp compression [36]—or may involve complex structural coexistence, such as the simultaneous presence of amorphous and crystalline domains in vitreous water [37]. To robustly track the structural evolution during and after simulations, we employ three complementary phase identification methods, which are described in the following subsections.

We determine the dominant phase by combining local and global indicators. (i) Local symmetry [dynamical graph convolutional neural network (DGCNN)]: for the each ensemble we label a phase as dominant once it is the largest fraction. For isobaric ensemble this fraction exceeds 70% for $P42/nmc$, while for the constant-stress ensemble the $Pbcn$ phase fraction exceeds 80%. (ii) RDF: for each ramp we compare ensemble-averaged RDFs to pure-phase references at same conditions and assign the phase whose peaks best align as dominant for that ensemble. (iii) XRD: we take the top-probability class as dominant; at the end of the ramps the classifier confidence is typically >0.95.

For each atom in a configuration, the local-symmetry model outputs a probability distribution over candidate phases. We assign the atom to the phase with the highest score, then aggregate these atomic labels to obtain the fractional population of each phase in that configuration. The configuration's phase is finally labeled as the phase with the largest fractional value and is corroborated by both RDF and XRD classification methods. We note that mixed-phase states can be more realistic at high temperatures than sharp transitions considering that increased ion kinetics would enhance

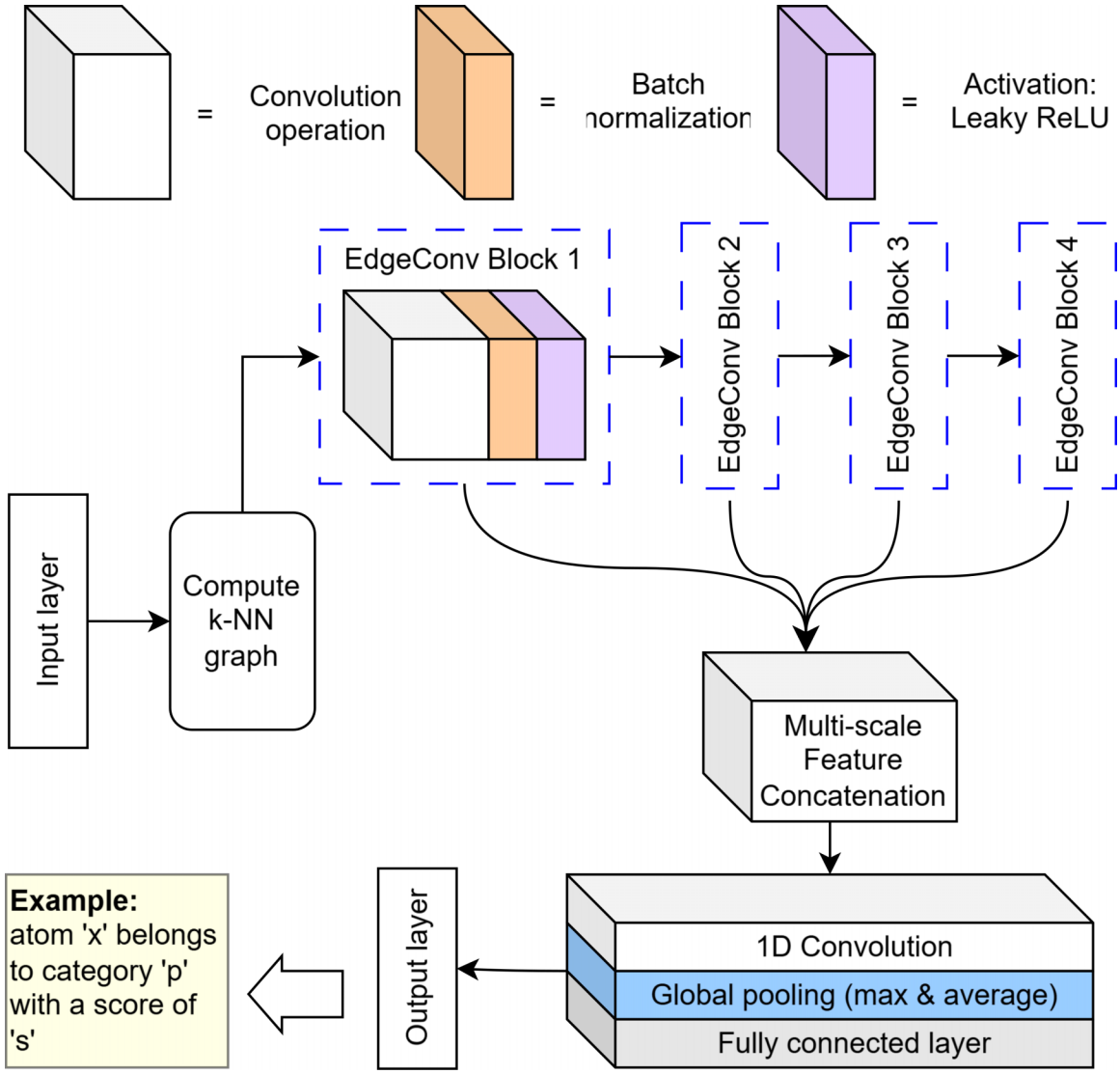

FIG. 5. Schematic of the DGCNN architecture. The model constructs a k-nearest neighbor graph and processes it through four stages of edge-convolution operations. The outputs from these convolutional stages are merged, and only the maximum and average responses are pooled to create a descriptor of each atom's local environment. This descriptor is then used to assign each atom to its corresponding class.

the probability of finding competing phases, according to the Boltzmann distribution. This is consistent with findings in other materials including MgO, which was experimentally observed to have mixed phases [38] and theoretically shown to have larger uncertainty in the B1–B2 phase boundary nearer to the triple point [39], and iron, which was predicted to have substantial coexistence of different phases due to their similar free energies and low transition barrier [40], at high pressure-temperature conditions relevant to planetary interiors.

3. Local symmetry identification model

We developed an ML model to identify local atomic symmetry. In large-scale MD simulations—especially at high temperatures and pressures—it is common to encounter mixed phases. Traditional methods, such as the Steinhardt bond order parameter [41], common neighbor analysis (CNA), Adaptive CNA, and polyhedral template matching, often fail when mixed or more complex phases are present [42,43]. Consequently, recent studies have adopted ML-based models as a more robust solution for classifying phases in systems with complex or mixed phases.

In our work, we employ a DGCNN model for this classification task. Wang *et al.* [44] introduced the DGCNN architecture for analyzing 3D point cloud data (i.e., sets of points in three-dimensional space representing objects, where DGCNN learns to capture local geometric relationships by dynamically building graphs among nearby points). Follow-up studies have shown that treating each atom's spatial coordinates as a "point cloud" enables DGCNN to learn detailed structural features of the material and assign each atom to its correct crystal phase. For example, this approach has been applied in a SiO_2 shock-loading simulation [45] to classify the complex phases of the material under extreme conditions during shock propagation. Our ML model utilizes the DGCNN architecture, as summarized in Fig. 5. For additional details on the model development and evaluation procedures, please refer to the Supplemental Material [26].

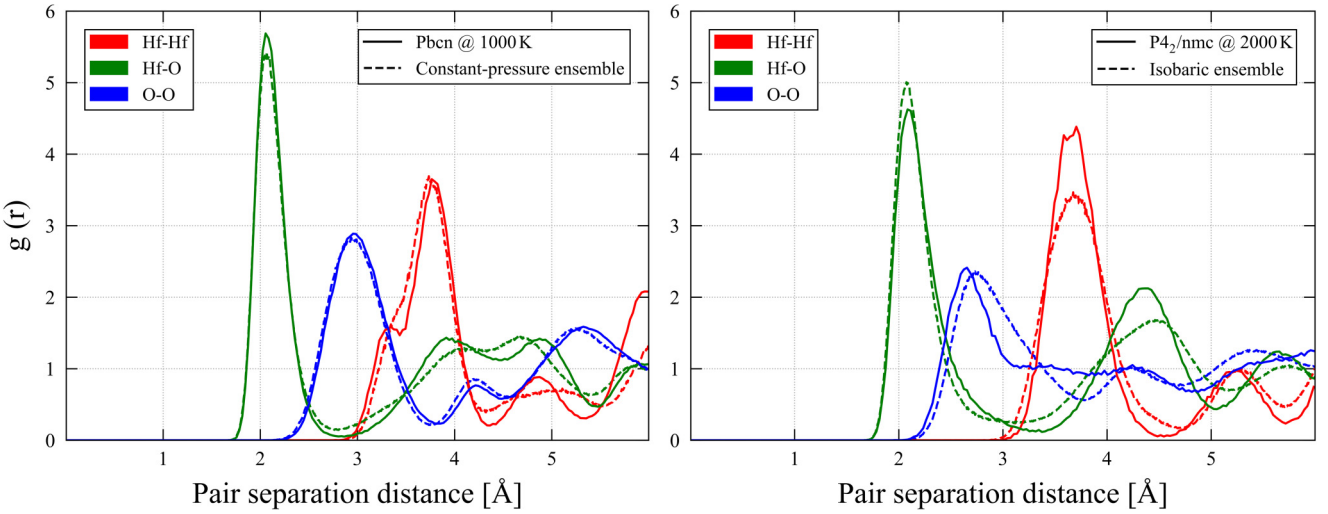

FIG. 6. Comparison of Radial distribution functions (RDFs)–Left: constant-stress ensemble and pure *Pbcn* phase, both at ∼1000 K and 0 GPa. Right: isobaric ensemble and pure $P4_2/nmc$ phase, both at ∼2000 K and 0 GPa. The systems were first equilibrated for 120 ps, followed by time-averaging of the RDFs to ensure statistical reliability.

Starting from input atom coordinates, the model first builds a k-nearest neighbor graph to capture local relationships between points. Each EdgeConv block then applies a small convolution-like operation on the edges of this graph, learning how each point relates to its neighbors. Outputs from multiple EdgeConv layers are merged to collect information at different neighborhood sizes. A 1D convolution is applied to the concatenated features to further mix information across the point dimension, and a global pooling step (taking both the maximum and the average over all points) reduces the point-wise features into a single descriptor for the atomic environment. Finally, a fully connected layer transforms this descriptor into class scores, so that each atom can be classified into its correct phase or category.

The dataset comprises eight distinct phases of HfO_2, including fully relaxed structures from the Materials Project [46] and perturbed versions with up to 5% atomic displacement to mimic thermal fluctuations and improve model robustness. These structures are replicated along crystallographic axes, resulting in a dataset of approximately one million atoms. The data is divided into training and hold-out test sets with a 9:1 ratio.

Applying our trained local-symmetry identification model to the final configurations obtained from isobaric and constant-stress simulations reveals that the choice of stress ensemble has a significant impact on the resulting crystal phase. In the isobaric ensemble—where a purely deviatoric stress is imposed—approximately 70% of the atoms adopt the tetragonal $P4_2/nmc$ structure. By contrast, in the constant-stress ensemble—under zero applied stress—about 80% of the atoms transform into the orthorhombic *Pbcn* phase. Thus, deviatoric stress conditions favor the $P4_2/nmc$ phase, while zero-stress conditions favor the tetragonal *Pbcn* phase.

4. Radial distribution function

Radial Distribution Function is a helpful tool for identifying phase transitions by analyzing atomic-level structural arrangements. RDF measures the probability of finding a particle at a given distance from a reference particle, allowing us to distinguish between different solid phases based on their unique RDF signatures. To determine the phases using RDF, we first generate pure-phase reference structures for the *Pbcn* and $P4_2/nmc$ phases at elevated temperatures by simulating each in an NPT ensemble (Fig. 6). We then extracted equilibrated configurations at the same temperatures from temperature-ramping simulations started with the $Pca2_1$ phase, run under both isobaric and constant-stress ensembles, as described earlier. Then we computed radial distribution functions for all systems—both the pure-phase references and the post-ramp configurations—and directly compared the resulting curves.

The left panel of Fig. 6 demonstrates strong agreement between the RDFs of the constant stress ensemble and the pure *Pbcn* phase of HfO_2, indicating that the resulting simulation cell predominantly consists of the *Pbcn* phase. Nearly all peaks in both the pure *Pbcn* phase and the constant-stress simulation RDFs are well aligned. While RDF plots do not provide a precise quantification of phase distribution in the final configuration, the close match strongly suggests that the system is primarily in the *Pbcn* phase at the given temperature. Similarly, the comparison between the RDFs of the isobaric ensemble and the pure $P4_2/nmc$ phase at 2000 K (right panel of Fig. 6) suggests that the resulting system mainly consists of the $P4_2/nmc$ phase.

5. XRD classification model

To address the challenges associated with detecting subtle, thermally induced phase transitions, we developed a machine learning model that classifies HfO_2 phases based on their XRD patterns. Importantly, this method provides global-level phase identification rather than local symmetry identification because XRD produces a single diffraction signature that represents an average over all atoms in the system, rather than focusing on individual atomic environments. Our

approach leverages a no-pooling convolutional neural network (NPCNN) [47] architecture, which preserves the complete spatial resolution of the XRD data by eliminating pooling operations. This design enables the model to effectively capture fine peak-level variations characteristic of subtle structural changes [48]. Specifically, the network consists of three sequential one-dimensional convolutional layers, each accompanied by a ReLU activation and a dropout rate of 30% to mitigate overfitting. The resulting feature maps are then flattened and passed to a fully connected layer that performs eight-way classification. The architecture of the model, as shown in Fig. 9 is mainly adopted by the XRD classification model, which was previously developed by our group and published in the literature [48].

Starting from crystallographic information files (CIFs) in the inorganic crystal structure database (ICSD) [49], we assembled a dataset of 1,296 unique XO_2-type (where X = Hf, Zr, Ti, etc.) structures belonging to eight space groups—14 ($P2_1/c$), 29 ($Pca2_1$), 60 ($Pbcn$), 61 ($Pbca$), 62 ($Pnma$), 137 ($P4_2/nmc$), and 225 ($Fm\bar{3}m$)—which are commonly associated with HfO_2. Each group contains the same number of entries to eliminate any bias in the training set, and those structures belong to both 0 K theoretical and non-zero-temperature experimental data. We simulated their XRD patterns, which were then input as the training dataset of the model. Most ICSD entries represent ambient-temperature structures. However, high-temperature simulations introduce significant atomic vibrations that can cause small but systematic peak shifts in the diffraction patterns [50]. To mimic this effect, we implemented a controlled peak-shifting protocol—allowing each diffraction peak to vary within a narrow, predefined range. After training with 6,480 augmented samples, the model achieved an accuracy of 86.34% on the test dataset. (see Sec. D of the Computational Methods and the Supplemental Material [26] for more details).

At the end of each temperature ramping simulation, we generated the corresponding XRD pattern and applied our XRD classifier to predict the belonging phase. The model's predictions align with our previous structural analysis: under isobaric ensemble, the system adopts a $P4_2/nmc$ phase, whereas under the constant-stress ensemble, it adopts the $Pbcn$ phase. In both scenarios, the classifier identifies the correct phase with over 95% confidence.

C. Influence of stress state on phase stability

By plotting enthalpy as a function of temperature, we can determine which phase is thermodynamically most stable at each temperature—the phase with the lowest enthalpy is the most favorable. This approach enables direct comparison of phase stability and reveals transitions under varying stress conditions. In our classical NPT MD simulations of HfO_2, the crystal's internal energy $U(T)$ is composed of a potential-energy term that represents the electronic/chemical-bond landscape encoded in the interatomic potential, and a kinetic energy term that increases with temperature due to lattice vibrations (phonons). However, since we run at finite temperatures yet keep the external pressure essentially zero, the enthalpy $H = U + PV$ reduces to $H \simeq U$; consequently, a first-order structural transition appears as a discontinuity in the total energy trajectory. This discontinuity corresponds to the latent heat absorbed or released during the phase transformation, reflecting a sudden reorganization of atomic configurations. A representative plot illustrating this energy jump—indicative of a first-order transition—is provided in the Supplemental Material [26] (Fig. S1).

The enthalpy–temperature plot (Fig. 7) illustrates that at elevated temperatures, the enthalpy of the system simulated under the constant-stress ensemble closely matches that of the pure $Pbcn$ reference phase equilibrated under identical temperature conditions. This alignment suggests that the structure in the constant-stress ensemble predominantly adopts or maintains a high concentration of the $Pbcn$ phase. Conversely, the enthalpy values from the isobaric ensemble simulations align more closely with those of the tetragonal ($P4_2/nmc$) reference phase, which is also equilibrated under the same conditions, indicating a clear preference for the tetragonal phase. Thus, the choice of the ensemble significantly influences the phase stability and the thermodynamic pathways accessible to the $Pca2_1$ phase of HfO_2. We complemented the enthalpy analysis with Helmholtz free-energy calculations along both simulation paths. At comparable temperatures, the isobaric path exhibits a higher free energy than the constant-stress path. The difference arises from the constraint structure: in the isobaric ensemble, the cell is stress-coupled across the three directions (box vectors change in a coupled way), which reduces effective configurational degrees of freedom and raises the free energy; in the constant-stress ensemble, each normal stress component is controlled independently, and the box vectors relax independently during MD, increasing the accessible phase space and lowering the free energy. This thermodynamic preference is consistent with the ensemble-dependent phase selection inferred from Fig. 7.

Even when the mean (hydrostatic) stress is zero, the non-zero normal components in the stress tensor can strongly affect the phase that HfO_2 adopts. In an isobaric ensemble, the simulation is set up to have a net pressure of zero (i.e., the trace of the stress tensor sums to zero), but the normal stresses along individual crystallographic directions may not be equal. In other words, there is residual stress in the plane even though the overall pressure is zero.

Although our NPT simulations keep the average (hydrostatic) pressure at zero in the isobaric ensemble using a Nosé–Hoover barostat, they do not guaranty that each normal component of the stress tensor is also zero. We observe residual in-plane stress in the 6,144-atom supercell simulations, with $\sigma_{xx} \approx +3$ GPa and $\sigma_{yy} \approx -3$ GPa, while $\sigma_{zz} \approx 0$ GPa (see Fig. S2 in the Supplemental Material [26]). This means the crystal experiences compression along one in-plane direction and tension along the perpendicular in-plane direction, despite having zero net pressure overall. Because HfO_2 has several polymorphs whose energies differ by only a few meV per unit cell, even this modest directional stress can drive the free-energy balance toward the $P4_2/nmc$ phase, whose lattice naturally prefers one long and two short axes. The system therefore tends to transition into the $P4_2/nmc$ structure whenever such residual in-plane stresses are present.

Fan *et al.* showed that the apparent divergence between PBE and PBEsol predictions for the $Pca2_1$–HfO_2 transformation pathways is largely due to their mechanical boundary

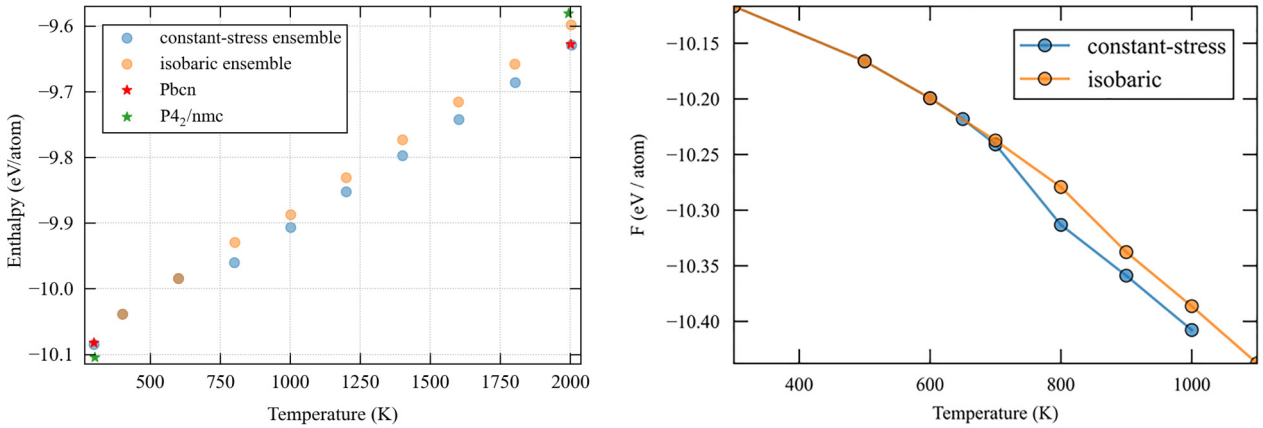

FIG. 7. Left: enthalpy of the system of the two ensembles as a function of temperature. The graph includes (marked with stars) systems containing pure $P4_2/nmc$ and $Pbcn$ phases as reference points. Right: Helmholtz free energy of the two ensembles at comparable temperatures.

conditions. PBE stabilizes *Pbcn* at larger volumes and lower density, while PBEsol favors $Pca2_1$ and $P4_2/nmc$. When the mechanical boundary is fixed, for example with the lattice held at the $Pca2_1$ ground state, all three functionals PBE, PBEsol, and HSE yield consistent relative stabilities and switching barriers [20]. In other words, the choice of functional determines the effective position along the strain–volume axis; by adjusting the mechanical constraint (stress or strain), one can reproduce the pathway of the other functional. Our results follow the same picture. Isobaric runs carry residual deviatoric stresses with roughly $\sigma_{xx} \approx +3$ GPa, $\sigma_{yy} \approx -3$ GPa, $\sigma_{zz} \approx 0$ that bias the lattice toward $P4_2/nmc$, whereas constant stress runs enforce $\sigma_{xx} = \sigma_{yy} = \sigma_{zz} = 0$, remove the directional bias, and allow *Pbcn* to emerge. Thus, selective controlling of the applied stress is not arbitrary, and it deliberately moves our PBE trained model to the same endpoints identified by Fan *et al.*, yielding the same transformation without changing the exchange–correlation functional.

The mechanism is geometric: Starting from orthorhombic $Pca2_1$, a positive stress along a and negative stress along b drive a decrease of the a axis and an increase of the b axis until they become comparable ($a \approx b$), which favors the tetragonal lattice. This stress selection effect aligns with the ensemble dependent behavior explained by our enthalpy-temperature and reference phase comparisons.

By contrast, in the constant-stress ensemble run, we use a Nosé–Hoover barostat to drive every diagonal stress component (σ_{xx}, σ_{yy}, σ_{zz}) to zero while allowing all cell lengths and angles to relax freely (Parrinello–Rahman style). With no directional bias left, the free-energy landscape reorganizes and the orthorhombic *Pbcn* polymorph can emerge as the most stable outcome. This *Pbcn* phase is penalized by the unequal stresses in the previous (isobaric) ensemble. These trends are quantitatively supported by our free-energy comparison, which places the constant-stress path lower in F(T) than the isobaric path at comparable temperatures, consistent with Fig. 7 and the measured residual stresses.

While our free-energy comparisons establish thermodynamic preference along the two paths, they do not by themselves quantify kinetic accessibility. Assessing barriers requires pathway sampling between phases. At 0 K, this could be estimated with Nudge Elastic Band type calculations; at finite temperature, appropriate approaches include enhanced-sampling methods (e.g., metadynamics) to obtain free energies of intermediate states. Implementing such finite-T pathway calculations is a focus of our ongoing work, and we have noted this limitation and anticipate to work on this problem as a part of our future work.

Although our simulations target pure bulk HfO_2, most finite-temperature experimental observations of $Pca2_1$-related transitions are on doped bulk hafnia. Within that scope difference, our transition scales are consistent in magnitude with experiments: starting from $Pca2_1$, the isobaric path transforms to $P4_2/nmc$ at ∼1000 K, whereas the constant-stress path transforms to *Pbcn* at ∼800 K. For comparison, bulk Lu-doped $Hf_{0.6}Zr_{0.4}O_2$ shows heating transformations to $P4_2/nmc$ around 600–700 °C (≈ 873–973 K) [17], and bulk Lu-doped HfO_2 and Y-doped HfO_2 report windows near 900–1000 °C and ∼800 °C [10], respectively.

Mechanistically, this agreement is sensible due to two reasons. (i) dopants such as Lu, Y, and Zr are known to stabilize nonmonoclinic polymorphs and lower effective transformation temperatures, and (ii) nonhydrostatic stress biases the pathway toward tetragonal, as also demonstrated experimentally where pressure/stress cycling can access specific polymorphs in doped hafnia [51]. In our work, the isobaric ensemble develops residual deviatoric stresses, which favor the $P4_2/nmc$ phase at around 1000 K. Conversely, the constant-stress ensemble removes that directional bias, favoring *Pbcn* at a lower temperature (≈ 800 K). We therefore present the experimental comparison as a qualitative cross-check that supports the ordering and stress sensitivity that we find for pure HfO_2.

III. CONCLUSIONS

In this study, we developed a machine learning-based interatomic potential for HfO_2, which accurately predicted structural, mechanical, and thermodynamic properties across multiple polymorphs. The MLIP closely matched density functional theory data, demonstrating strong agreement in lattice parameters, bulk and shear moduli, and elastic con-

stants at different pressures, and the equation of state. It also successfully predicted mechanical properties for HfO_2 phases that were not included in the training dataset. This capability highlights the model's transferability, making it a powerful tool for exploring new and metastable phases of HfO_2 without relying on expensive quantum mechanical calculations.

Under isobaric ensemble, the energy pathways of the system are more favorable toward the $P4_2/nmc$ phase. This transition occurs with the system exhibiting residual stress along the x and y directions, even though the overall pressure averages to zero, meaning that the system is at a purely deviatoric stress state. Conversely, under the constant-stress ensemble, the system favors a *Pbcn*-rich mixture with no residual stress (zero stress state). This suggests that phase stability depends not only on the mean pressure but also on the distribution of stress components: deviatoric stress can alter the free-energy landscape to stabilize polymorphs inaccessible under uniform loading. These results emphasize how residual stresses along different crystallographic directions influence phase transformation pathways, a factor that previous studies often overlooked. To ensure precise phase identification, we combined local symmetry detection, radial distribution function analysis, enthalpy comparison, and x-ray diffraction pattern-based classification, allowing us to comprehensively analyze structural changes under varying conditions.

Beyond validating the MLIP, we show how machine learning-driven approaches enhance materials science by balancing computational efficiency with quantum mechanical accuracy. Moreover, we emphasize that relying on a single identification method is often insufficient—particularly when mixed phases emerge within the same simulation cell—so we introduced and developed accurate machine learning techniques capable of distinguishing coexisting structures. Our findings offer critical insights into the thermodynamic landscape of ferroelectric HfO_2.

We intentionally focused this study on a baseline MLIP for pure HfO_2 to analyze temperature-driven phase transitions under controlled stress states. The developed MLIP can be further refined to investigate dopant effects in HfO_2, enabling prediction of how substitutional and interstitial impurities influence phase stability and ferroelectric behavior. For example, training sets that include Si, Zr, Y, La, and other common dopants can be used to model changes in energy barriers associated with ferroelectric switching, similar to approaches in high-throughput DFT studies of doped HfO_2 thin films [2,52]. Similarly, extending MLIPs to high-pressure regimes will enable us to explore pressure-induced phase diagrams. By incorporating pressure-dependent training data (e.g., MD trajectories at tens to hundreds of GPa), MLIPs can capture structural softening and predict new polymorphs that emerge at high pressures.

Moreover, ML-based structure identifiers—such as deep-learning classifiers applied to XRD patterns—could be integrated with MLIPs to enable real-time, high-throughput phase mapping during simulations and experiments. In the long term, such combined MLIP and ML-identifier approaches will accelerate the discovery of HfO_2-based materials with tailored ferroelectric, mechanical, or optical properties.

IV. COMPUTATIONAL METHODS

A. Machine learning interatomic potential

Interatomic potentials are developed with the DeepMD method [53], which is briefly discussed below. In a deep potential model, a fitting property of an atom is generally represented using a fitting network, which is a function of the descriptor:

$$y_i = \mathcal{F}(\mathcal{D}(\boldsymbol{x_i}, \{\boldsymbol{x_j}\}_{j\in n(i)}; \boldsymbol{\theta_d}); \boldsymbol{\theta_f}), \tag{1}$$

where y_i represents the predicted property for atom i, such as its potential energy or force. The input $\boldsymbol{x_i}$ is the feature vector for atom i, comprising its Cartesian coordinates r_i and chemical species α_i. The set $\{\boldsymbol{x_j}\}_{j\in n(i)}$ contains the feature vectors of neighboring atoms j within a cutoff radius, reflecting the local environment around atom i. The descriptor function $\mathcal{D}$, parameterized by $\boldsymbol{\theta_d}$, encodes this local environment into a form suitable for machine learning. The output of $\mathcal{D}$ is then passed to the fitting network $\mathcal{F}$, parameterized by $\boldsymbol{\theta_f}$, which produces the final prediction y_i. Using Eq. (1), if we set the target atomic property y_i to be the atomic energy E_i, the total potential energy of the system E can be expressed as the sum of the atomic energies: $E = \sum_i E_i$.

The loss function $L(p_\epsilon, p_f, p_\xi)$, as defined in Ref. [53], is used to train the DeepMD model by minimizing the differences between the predicted and reference data for energy, forces, and virial tensors:

$$L(p_\epsilon, p_f, p_\xi) = p_\epsilon \Delta\epsilon^2 + \frac{p_f}{3N}\sum_i |\Delta F_i| + \frac{p_\xi}{9}\|\Delta\xi\|^2. \tag{2}$$

The term $p_\epsilon \Delta\epsilon^2$ represents the contribution from the energy prediction error, where $\Delta\epsilon$ is the difference between the predicted and reference energies, and p_ϵ is a weighting factor. The term $\frac{p_f}{3N}\sum_i |\Delta F_i|$ accounts for the error in the predicted forces, where ΔF_i is the difference between the predicted and reference forces for atom i, N is the total number of atoms, and p_f is the corresponding weight.

Finally, $\frac{p_\xi}{9}\|\Delta\xi\|^2$ captures the error in the virial tensor prediction, where $\Delta\xi$ is the difference between the predicted and reference virial tensors, and p_ξ is the weight for this term. Each weighting parameter (p_ϵ, p_f, and p_ξ) controls the relative importance of energy, force, and virial tensor contributions in the training process.

For this work, we employed the Smooth Edition [54] of two-body embedding descriptor with angular information, capturing both radial and angular characteristics of the local atomic environment. It applies a cutoff radius of 6.0 Å with an additional smoothing length of 0.5 Å to ensure smooth behavior at the cutoff. The network structure consists of three hidden layers with 25, 50, and 100 neurons, respectively, complemented by an auxiliary axis network composed of 16 neurons. The energy fitting network was constructed using three hidden layers of 240 neurons each and used residual connections. Both networks are trained with double precision (float64) for numerical stability. Additionally, the loss function balanced contributions from energy, forces, and virials by dynamically adjusting their prefactors throughout the training process, which spanned 3 million steps with data drawn uniformly from a comprehensive set of DFT training and validation sets.

The dataset used for model development was drawn from an open-access repository for sharing datasets [23], which includes randomly perturbing ground-state structures of $P2_1/c$, $Pbca$, $Pca2_1$, and $P4_2/nmc$ phases of HfO_2. It comprises 27,149 frames generated via *ab initio* molecular dynamics (AIMD) NPT simulations spanning temperatures from 100 K to 3300 K and pressures from –50 kbar to 400 kbar. We randomly partitioned these frames into training and test sets in a 90:10 ratio to assess model performance. Although only four crystallographic phases of HfO_2 were included during training, we further tested the MLIP by evaluating it on previously unseen structures such as cubic ($Fm\bar{3}m$) and orthorhombic ($Pbcn$) phases to check its extrapolation capabilities. After the training, the model demonstrated strong convergence with a normalized energy RMSE of 1.60 meV and force and virial RMSEs (approximately 0.32 eV/Å and 0.028 eV/Å, respectively) for the validation set. To position our model within the recent HfO_2 MLIP literature, we include a summary table in the Supplemental Material [26] (Table S3) that compares frameworks, training-set scope, and test errors across Refs. [19,55–58]. Across shared metrics, our baseline HfO_2 potential achieves accuracy comparable to recent models developed with different ML frameworks.

B. Elastic constants calculations

Elastic constants (C_{ij}) of the $Pca2_1$ phase were computed with the MLIP and were compared with the DFT values at different pressures. We determined the nine independent elastic constants C_{ij} using an energy–strain finite–strain approach in both DFT and MLIP calculations. Starting from a fully relaxed reference cell, we generated nine symmetry-distinct deformations—three axial ($\varepsilon_{xx}, \varepsilon_{yy}, \varepsilon_{zz}$), three simple shears ($\varepsilon_{yz}, \varepsilon_{xz}, \varepsilon_{xy}$), with engineering shear magnitude γ set by the deformation parameter d ($\gamma = d$), and three volume-conserving orthorhombic pairs ($\varepsilon_{xx}, \varepsilon_{yy}$), ($\varepsilon_{xx}, \varepsilon_{zz}$), ($\varepsilon_{yy}, \varepsilon_{zz}$)—each applied with six magnitudes $d = \pm 0.6\%, \pm 1.2\%, \pm 1.8\%$. For every strained cell, lattice vectors were fixed while internal atomic positions were relaxed until forces were below 10^{-6} eV Å^{-1}. Total energies were then computed, and each elastic constant was obtained by fitting the corresponding energy–strain relation as explained in Eq. (3), using a quadratic fit around zero strain.

For our LAMMPS simulations, we constructed a $6 \times 6 \times 6$ supercell to ensure sufficient sampling of the material's response. We performed the same calculations with the Vienna Ab Initio Simulation Package (VASP) [59] to assess the accuracy of the developed MLIP, by comparing its predicted C_{ij} values with DFT results. The DFT calculations employed a 12-atom unit cell, an $8 \times 8 \times 8$ k-point mesh, a 600 eV energy cutoff, and used the projected augmented wave [60] method with the PBE functional within the GGA. The relationship between the applied strain ϵ and the resulting energy change ΔE in Voigt notation is given by

$$\Delta E = E(\epsilon) - E(0) = \frac{1}{2} V_0 \sum_{i,j} C_{ij} \epsilon_i \epsilon_j, \tag{3}$$

where V_0 is the equilibrium volume of the supercell, and C_{ij} are the elastic constants. By fitting the calculated energy-strain data to this quadratic form, the elastic constants C_{ij} were extracted.

C. Free-energy calculations

Helmholtz free energies were computed using the CALPHY [61] Python library via a nonequilibrium Hamiltonian interpolation along a Frenkel–Ladd path [62]. The system Hamiltonian is switched between our system and a reference Einstein crystal (harmonic oscillators) whose free energy can be computed analytically. A time-dependent coupling parameter λ in the range $0 \rightarrow 1$ is used for the switching during MD. Both forward (system $\rightarrow$ reference) and backward (reference $\rightarrow$ system) switching runs were performed to reduce bias from dissipated work. At each temperature, the system is equilibrated for 20 ps, then 30 ps of forward switching and 30 ps of backward switching are carried out under the same MD conditions as the production ramps. Ensemble definitions matched the main simulations (isobaric: $P = (\sigma_{xx} + \sigma_{yy} + \sigma_{zz})/3 = 0$ with nonzero normal components permitted; constant-stress: $\sigma_{xx} = \sigma_{yy} = \sigma_{zz} = 0$ with independent box relaxation).

D. Local symmetry Identification model

In large-scale classical MD simulations, materials often exhibit a range of local symmetries, with different regions adopting distinct phases simultaneously. While existing structure identification methods work well for simple or pure crystal structures, they struggle when dealing with complex or mixed phases, which are commonly encountered in high-pressure and high-temperature simulations. Developing a local symmetry identification model can address these challenges by detecting and characterizing the various symmetries present within a single simulation box.

The model is developed using the DGCNN [63] to learn from point cloud data. The dataset comprises eight distinct phases of HfO_2, including both fully relaxed and perturbed structures. These input structures are replicated along the crystallographic axes, resulting in a final dataset that contains approximately one million atoms.

The fully relaxed phases are sourced from "The Materials Project" database [46]. The perturbed systems are created by perturbing these structures by up to 5%, to mimic the random thermal fluctuations and thereby improve the robustness of the model. The final dataset is split into train and test (hold-out) sets with a ratio of 9:1. For detailed information on dataset generation, please refer to the Supplemental Material [26].

After combining all perturbed and fully relaxed structures, atomic clusters are extracted from each labeled system. The number of atoms in these clusters determines the input size for the model. To evaluate the model's performance across different input sizes, we trained four separate models with cluster sizes of 8, 16, 32, and 64 atoms, respectively.

The performance of the model on the test set (hold-out data) is summarized by the confusion matrix in Fig. 8. The final model is trained with input clusters of size 16.

E. XRD classifier

The NPCNN used in this study is a modified convolutional architecture designed to retain high-resolution features across

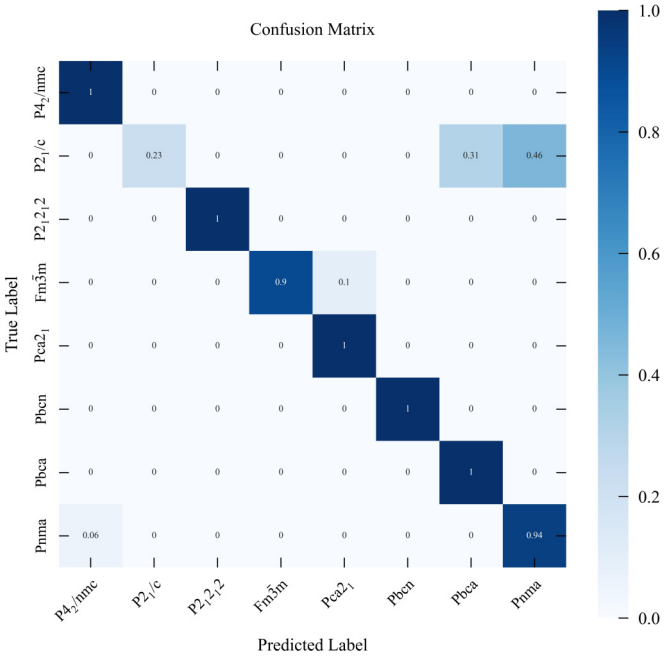

FIG. 8. Confusion matrix of the hold-out dataset for the model with input cluster size = 16.

all layers by removing traditional downsampling operations. As implemented, the NPCNN accepts a single-channel one-dimensional input and passes it through a sequence of three convolutional layers. The first layer applies 80 filters with a kernel size of 100 and a stride of 5, followed by a ReLU activation and a dropout layer with a rate of 0.3. This is followed by a second convolutional layer, also with 80 filters, using a kernel size of 50 and a stride of 5, again followed by ReLU and dropout. The third and final convolutional layer in the stack uses 80 filters with a kernel size of 25 and a stride of 2, followed by another ReLU activation and dropout. Notably, this architecture (Fig. 9) omits any form of pooling (e.g., average or max pooling), distinguishing it from conventional CNN designs. The absence of pooling layers ensures that spatial resolution is preserved throughout the network, which is especially beneficial for tasks such as x-ray diffraction pattern classification, where subtle features in the signal may carry important structural information [47,48]. The output of the NPCNN is subsequently flattened and passed into a fully connected predictor network for final classification [64,65]

To assemble the training set for our phase–classification model, we first retrieved CIFs corresponding to the eight most probable HfO_2 polymorphs of interest from the ICSD. For each phase, we collected 162 distinct XO_2-type structures (where X = Hf, Zr, Ti, etc.) distinct structures—predominantly characterized under ambient conditions—and used these CIFs to simulate their XRD patterns, yielding what we term the "original dataset." However, the number of data points collected was insufficient for robust model training.

The materials such as HfO_2, TiO_2, and ZrO_2—are all known to exhibit positive thermal expansion [66–68]. Given that our simulations were conducted at elevated temperatures, the interatomic distances are expected to increase. According to Bragg's law $n\lambda = 2d \sin\theta$, an increase in the interplanar spacing d leads to a decrease in the diffraction angle θ. Consequently, the peaks in the XRD pattern shift toward lower angles, a phenomenon that appears as a leftward shift. This temperature-induced peak shift has also been reported in the literature [50]. Therefore, to enhance the model's robustness against variations in experimental and thermal effects, we applied an augmentation procedure by applying controlled peak shifts to the "original dataset," thereby producing an expanded augmented dataset for classifier training. To achieve this objective, we applied leftward shifts to the "original dataset" to mimic thermal expansion effects. Specifically, peak positions were shifted by 0.05% to 0.5% toward lower angles to include the anticipated behavior under elevated temperatures.

ACKNOWLEDGMENTS

N.A., S.S., and Y.H.K. acknowledge funding from the U.S. Department of Energy (DOE), Office of Science (SC), and Fusion Energy Sciences, under Award No. DE-SC0020340. N.A. also acknowledges the support from the National Nuclear Security Administration via Grant No. NA0004078 and the National Science Foundation via Grant No. DMR2202124. N.A., Y.H.K., and S.S. acknowledge the support from the University Research Award from the University of Rochester. This material is partially based upon work supported by the Department of Energy (National Nuclear Security Administration) University of Rochester

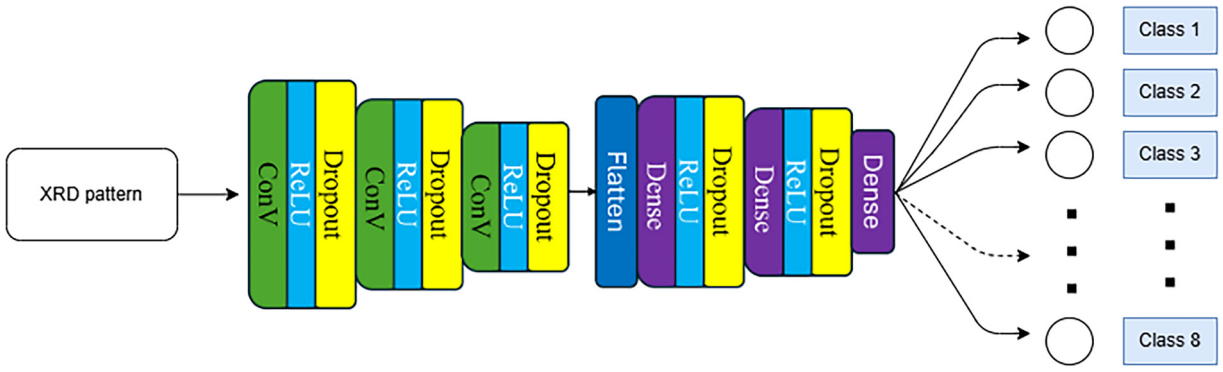

FIG. 9. No-pooling convolutional neural network (NPCNN) architecture. The input is the XRD pattern, and the output is the desired classification: eight space groups.

"National Inertial Confinement Fusion Program" under Award No. DE-NA0004144.

DATA AVAILABILITY

The data that support the findings of this article are openly available [69]; embargo periods may apply.

[1] D. Lehninger, F. Müller, Y. Raffel, S. Yang, M. Neuber, S. Abdulazhanov, T. Kämpfe, K. Seidel, and M. Lederer, Ferroelectric hafnium oxide: A potential game-changer for nanoelectronic devices and systems, Adv. Electron. Mater. **11**, 2400686 (2025).

[2] T. Zhu, L. Ma, S. Deng, and S. Liu, Progress in computational understanding of ferroelectric mechanisms in HfO_2, npj Comput. Mater. **10**, 188 (2024).

[3] J. Yuan, G. Mao, K. Xue, N. Bai, C. Wang, Y. Cheng, H. Lyu, H. Sun, X. Wang, and X. Miao, Ferroelectricity in HfO_2 from a chemical perspective, Chem. Mater. **35**, 94 (2023).

[4] T. D. Huan, V. Sharma, G. A. Rossetti Jr, and R. Ramprasad, Pathways towards ferroelectricity in hafnia, Phys. Rev. B **90**, 064111 (2014).

[5] T. S. Böscke, J. Müller, D. Bräuhaus, U. Schröder, and U. Böttger, Ferroelectricity in hafnium oxide thin films, Appl. Phys. Lett. **99**, 102903 (2011).

[6] T. Mikolajick and U. Schroeder, Ferroelectricity in bulk hafnia, Nat. Mater. **20**, 718 (2021).

[7] Q. Shi, E. Parsonnet, X. Cheng, N. Fedorova, R.-C. Peng, A. Fernandez, A. Qualls, X. Huang, X. Chang, H. Zhang, *et al.*, The role of lattice dynamics in ferroelectric switching, Nat. Commun. **13**, 1110 (2022).

[8] Q. Luo, Y. Cheng, J. Yang, R. Cao, H. Ma, Y. Yang, R. Huang, W. Wei, Y. Zheng, T. Gong, *et al.*, A highly CMOS compatible hafnia-based ferroelectric diode, Nat. Commun. **11**, 1391 (2020).

[9] S.-J. Jeong, Y. Gu, J. Heo, J. Yang, C.-S. Lee, M.-H. Lee, Y. Lee, H. Kim, S. Park, and S. Hwang, Thickness scaling of atomic-layer-deposited HfO_2 films and their application to wafer-scale graphene tunnelling transistors, Sci. Rep. **6**, 20907 (2016).

[10] X. Xu, F.-T. Huang, Y. Qi, S. Singh, K. M. Rabe, D. Obeysekera, J. Yang, M.-W. Chu, and S.-W. Cheong, Kinetically stabilized ferroelectricity in bulk single-crystalline HfO_2: Y, Nat. Mater. **20**, 826 (2021).

[11] Y. Qi, S. Singh, C. Lau, F.-T. Huang, X. Xu, F. J. Walker, C. H. Ahn, S.-W. Cheong, and K. M. Rabe, Stabilization of competing ferroelectric phases of HfO_2 under epitaxial strain, Phys. Rev. Lett. **125**, 257603 (2020).

[12] T. Rahman, A. F. Khan, and N. Nawal, Analysis of NCFET with Si doped HfO_2 as ferro-electric material to achieve lower SS, in *Proceedings of the 1st International Conference on Advances in Science, Engineering and Robotics Technology (ICASERT)* (IEEE, Piscataway, NJ, USA, 2019).

[13] Z. Fan, J. Chen, and J. Wang, Ferroelectric HfO_2-based materials for next-generation ferroelectric memories, J. Adv. Dielectr. **06**, 1630003 (2016).

[14] A. Reinhardt, Phase behavior of empirical potentials of titanium dioxide, J. Chem. Phys. **151**, 064505 (2019).

[15] C. Verdi, F. Karsai, P. Liu, R. Jinnouchi, and G. Kresse, Thermal transport and phase transitions of zirconia by on-the-fly machine-learned interatomic potentials, npj Comput. Mater. **7**, 156 (2021).

[16] LAMMPS, Fix nvt command: https://docs.lammps.org/fix_nh.html.

[17] S. Wang, Y. Shen, X. Yang, P. Nan, Y. He, N. Lu, H. Yu, B. Ge, S. Zhang, and H. Zhang, Unlocking the phase evolution of the hidden non-polar to ferroelectric transition in HfO_2-based bulk crystals, Nat. Commun. **16**, 3745 (2025).

[18] S. Liu and B. M. Hanrahan, Effects of growth orientations and epitaxial strains on phase stability of HfO_2 thin films, Phys. Rev. Mater. **3**, 054404 (2019).

[19] J. Wu, Y. Zhang, L. Zhang, and S. Liu, Deep learning of accurate force field of ferroelectric HfO_2, Phys. Rev. B **103**, 024108 (2021).

[20] D. Fan, T. Zhu, and S. Liu, Unexpected density functional dependence of the antipolar *Pbcn* phase in HfO_2, npj Comput. Mater. **11**, 1 (2025).

[21] J. Wu, J. Yang, L. Ma, L. Zhang, and S. Liu, Modular development of deep potential for complex solid solutions, Phys. Rev. B **107**, 144102 (2023).

[22] J. Zeng, D. Zhang, D. Lu, P. Mo, Z. Li, Y. Chen, M. Rynik, L. Huang, Z. Li, S. Shi, *et al.*, DeePMD-kit v2: A software package for deep potential models, J. Chem. Phys. **159**, 054801 (2023).

[23] AIS Square, https://www.aissquare.com/.

[24] C. E. Curtis, L. M. Doney, and J. R. Johnson, Some properties of hafnium oxide, hafnium silicate, calcium hafnate, and hafnium carbide, J. Am. Ceram. Soc. **37**, 458 (1954).

[25] D. W. Stacy and D. R. Wilder, The yttria-hafnia system, J. Am. Ceram. Soc. **58**, 285 (1975).

[26] See Supplemental Material at http://link.aps.org/supplemental/10.1103/gkvf-t1vl for MD temperature-ramping and stress analyses, benchmark comparisons to DFT (elastic constants, lattice constants, energy/force/stress predictions), descriptions and evaluations of symmetry and XRD classifiers, a literature comparison of MLIP accuracy, and bond-length analysis with figures and tables.

[27] A. P. Thompson, H. M. Aktulga, R. Berger, D. S. Bolintineanu, W. M. Brown, P. S. Crozier, P. J. in 't Veld, A. Kohlmeyer, S. G.

Moore, T. D. Nguyen, R. Shan, M. J. Stevens, J. Tranchida, C. Trott, and S. J. Plimpton, LAMMPS—A flexible simulation tool for particle-based materials modeling at the atomic, meso, and continuum scales, Comput. Phys. Commun. **271**, 108171 (2022).

[28] R. Ruh and P. W. R. Corfield, Crystal structure of monoclinic hafnia and comparison with monoclinic zirconia, J. Am. Ceram. Soc. **53**, 126 (1970).

[29] M. Hoffmann, U. Schroeder, T. Schenk, T. Shimizu, H. Funakubo, O. Sakata, D. Pohl, M. Drescher, C. Adelmann, R. Materlik, A. Kersch, and T. Mikolajick, Stabilizing the ferroelectric phase in doped hafnium oxide, J. Appl. Phys. **118**, 072006 (2015).

[30] I. MacLaren, T. Ras, M. MacKenzie, A. J. Craven, D. W. McComb, and S. De Gendt, Texture, twinning, and metastable "tetragonal" phase in ultrathin films of HfO_2 on a Si substrate, J. Electrochem. Soc. **156**, G103 (2009).

[31] Q.-J. Hong, S. V. Ushakov, D. Kapush, C. J. Benmore, R. J. K. Weber, A. Van De Walle, and A. Navrotsky, Combined computational and experimental investigation of high temperature thermodynamics and structure of cubic ZrO_2 and HfO_2, Sci. Rep. **8**, 14962 (2018).

[32] F. Birch, Finite elastic strain of cubic crystals, Phys. Rev. **71**, 809 (1947).

[33] A. Alvarez, N. Abdolrahim, and S. Singh, Anomalous elastic softening in ferroelectric hafnia under pressure, Phys. Rev. B **111**, 064106 (2025).

[34] J. L. Musfeldt, S. Singh, K. A. Smith, X. Xu, S.-W. Cheong, Z. Liu, D. Vanderbilt, and K. M. Rabe, Pressure-driven polar orthorhombic to tetragonal phase transition in hafnia at room temperature, Chem. Mater. **37**, 1820 (2025).

[35] A. Stukowski, Visualization and analysis of atomistic simulation data with OVITO—the open visualization tool, Modell. Simul. Mater. Sci. Eng. **18**, (2010).

[36] L. He, D. Polsin, S. Zhang, G. W. Collins, and N. Abdolrahim, Phase transformation path in aluminum under ramp compression; Simulation and experimental study, Sci. Rep. **12**, 18954 (2022).

[37] A. K. Shargh, A. Picard, R. Hrubiak, D. Zhang, R. J. Hemley, S. Deemyad, N. Abdolrahim, and S. Saffarian, Coexistence of vitreous and crystalline phases of H_2O at ambient temperature, Proc. Natl. Acad. Sci. USA **119**, e2117281119 (2022).

[38] J. K. Wicks, S. Singh, M. Millot, D. E. Fratanduono, F. Coppari, M. G. Gorman, Z. Ye, J. R. Rygg, A. Hari, J. H. Eggert, *et al.*, B1-B2 transition in shock-compressed MgO, Sci. Adv. **10**, eadk0306 (2024).

[39] S. Zhang, R. Paul, S. X. Hu, and M. A. Morales, Toward an accurate equation of state and B1-B2 phase boundary for magnesium oxide up to terapascal pressures and electron-volt temperatures, Phys. Rev. B **107**, 224109 (2023).

[40] S. Zhang, A. Panjwani, P. Xiao, M. Ghosh, T. Ogitsu, Y. Ping, and S. X. Hu, Thermally induced structural competitiveness and metastability of body-centered-cubic iron under nonequilibrium conditions, Phys. Rev. B **111**, 224106 (2025).

[41] P. J. Steinhardt, D. R. Nelson, and M. Ronchetti, Bond-orientational order in liquids and glasses, Phys. Rev. B **28**, 784 (1983).

[42] S. Pan, J. Shi, Z. Liang, C. Liu, J. Wang, Y. Wang, H.-T. Wang, D. Xing, and J. Sun, Shock compression pathways to pyrite silica from machine learning simulations, Phys. Rev. B **110**, 224101 (2024).

[43] B. D. Snow, D. D. Doty, and O. K. Johnson, A simple approach to atomic structure characterization for machine learning of grain boundary structure-property models, Front. Mater. **6**, 120 (2019).

[44] Y. Wang, Y. Sun, Z. Liu, S. E. Sarma, M. M. Bronstein, and J. M. Solomon, Dynamic graph CNN for learning on point clouds, ACM Trans. Graphics (TOG), **38**, 1 (2019).

[45] L. C. Erhard, D. Utt, A. J. Klomp, and K. Albe, Crystal structure identification with 3D convolutional neural networks with application to high-pressure phase transitions in SiO_2, Modell. Simul. Mater. Sci. Eng. **32**, 065029 (2024).

[46] A. Jain, S. P. Ong, G. Hautier, W. Chen, W. D. Richards, S. Dacek, S. Cholia, D. Gunter, D. Skinner, G. Ceder, and K. A. Persson, Commentary: The materials project: A materials genome approach to accelerating materials innovation, APL Mater. **1**, 011002 (2013).

[47] J. T. Springenberg, A. Dosovitskiy, T. Brox, and M. Riedmiller, Striving for simplicity: The all convolutional net, arXiv:1412.6806.

[48] J. E. Salgado, S. Lerman, Z. Du, C. Xu, and N. Abdolrahim, Automated classification of big X-ray diffraction data using deep learning models, npj Comput. Mater. **9**, 214 (2023).

[49] M. Hellenbrandt, The inorganic crystal structure database (ICSD)—Present and future, Crystallogr. Rev. **10**, 17 (2004).

[50] N. M. Sultan, T. M. B. Albarody, H. K. M. Al-Jothery, M. A. Abdullah, H. G. Mohammed, and K. O. Obodo, Thermal expansion of 3C-SiC obtained from *in-situ* X-ray diffraction at high temperature and first-principal calculations, Materials **15**, 6229 (2022).

[51] J. L. Musfeldt, S. Singh, S. Fan, Y. Gu, X. Xu, S.-W. Cheong, Z. Liu, D. Vanderbilt, and K. M. Rabe, Structural phase purification of bulk HfO_2 :Y through pressure cycling, Proc. Natl. Acad. Sci. USA **121**, e2312571121 (2024).

[52] M. Falkowski, C. Künneth, R. Materlik, and A. Kersch, Unexpectedly large energy variations from dopant interactions in ferroelectric HfO_2 from high-throughput *ab initio* calculations, npj Comput. Mater. **4**, 73 (2018).

[53] H. Wang, L. Zhang, J. Han, and W. E, Deepmd-kit: A deep learning package for many-body potential energy representation and molecular dynamics, Comput. Phys. Commun. **228**, 178 (2018).

[54] L. Zhang, J. Han, H. Wang, W. Saidi, R. Car, *et al.*, End-to-end symmetry preserving inter-atomic potential energy model for finite and extended systems, Adv. Neural Info. Proc. Sys. **31** (2018).

[55] G. Sivaraman, A. N. Krishnamoorthy, M. Baur, C. Holm, M. Stan, G. Csányi, C. Benmore, and Á. Vázquez-Mayagoitia, Machine-learned interatomic potentials by active learning: Amorphous and liquid hafnium dioxide, npj Comput. Mater. **6**, 104 (2020).

[56] H. Zhang, X. Gu, Z. Fan, and H. Bao, Vibrational anharmonicity results in decreased thermal conductivity of amorphous HfO_2 at high temperature, Phys. Rev. B **108**, 045422 (2023).

[57] H. Chen, Y. Zhang, C. Zhou, and Y. Zhou, Deep learning potential model of displacement damage in hafnium oxide ferroelectric films, npj Comput. Mater. **10**, 270 (2024).

[58] G. Sivaraman, L. Gallington, A. N. Krishnamoorthy, M. Stan, G. Csányi, A. Vázquez-Mayagoitia, and C. J. Benmore, Ex-

perimentally driven automated machine-learned interatomic potential for a refractory oxide, Phys. Rev. Lett. **126**, 156002 (2021).

[59] G. Kresse and J. Furthmüller, Efficient iterative schemes for *ab initio* total-energy calculations using a plane-wave basis set, Phys. Rev. B **54**, 11169 (1996).

[60] P. E. Blöchl, Projector augmented-wave method, Phys. Rev. B **50**, 17953 (1994).

[61] S. Menon, Y. Lysogorskiy, J. Rogal, and R. Drautz, Automated free-energy calculation from atomistic simulations, Phys. Rev. Mater. **5**, 103801 (2021).

[62] D. Frenkel and A. J. C. Ladd, New Monte Carlo method to compute the free energy of arbitrary solids. Application to the fcc and hcp phases of hard spheres, J. Chem. Phys. **81**, 3188 (1984).

[63] Y. Wang, Y. Sun, Z. Liu, S. E. Sarma, M. M. Bronstein, and J. M. Solomon, Dynamic graph CNN for learning on point clouds, ACM Trans. Graph. **38**, (2019).

[64] P. M. Vecsei, K. Choo, J. Chang, and T. Neupert, Neural network based classification of crystal symmetries from X-ray diffraction patterns, Phys. Rev. B **99**, 245120 (2019).

[65] A. Zafar, M. Aamir, N. Mohd Nawi, A. Arshad, S. Riaz, A. Alruban, A. K. Dutta, and S. Almotairi, A comparison of pooling methods for convolutional neural networks, Appl. Sci. **12**, (2022).

[66] J. J. Low, N. H. Paulson, M. D'Mello, and M. Stan, Thermodynamics of monoclinic and tetragonal hafnium dioxide (HfO_2) at ambient pressure, Calphad **72**, 102210 (2021).

[67] D. R. Hummer, P. J. Heaney, and J. E. Post, Thermal expansion of anatase and rutile between 300 and 575 k using synchrotron powder X-ray diffraction, Powder Diffr. **22**, 352 (2007).

[68] X. Song, Y. Ding, J. Zhang, C. Jiang, Z. Liu, C. Lin, W. Zheng, and Y. Zeng, Thermophysical and mechanical properties of cubic, tetragonal and monoclinic ZrO2, J. Mater. Res. Technol. **23**, 648 (2023).

[69] GitHub Repo, https://github.com/niaz60/MLIPs.git.